

## Research Article

# Effects of Crystal Orientation and Grain Boundary Inclination on Stress Distribution in Bicrystal Interface of Austenite Stainless Steel 316L

Fu-qiang Yang <sup>1</sup>, He Xue <sup>2</sup>, Ling-yan Zhao <sup>1</sup>, Xiu-Rong Fang <sup>2</sup>,  
and Hai-bing Zhang <sup>3</sup>

<sup>1</sup>School of Science, Xi'an University of Science & Technology, Xi'an 710054, China

<sup>2</sup>School of Mechanical Engineering, Xi'an University of Science & Technology, Xi'an 710054, China

<sup>3</sup>State Key Laboratory for Marine Corrosion and Protection, Luoyang Ship Material Research Institute (LSMRI), Qingdao 266237, China

Correspondence should be addressed to Fu-qiang Yang; yang\_afreet@163.com and Hai-bing Zhang; zhanghb@sunrui.net

Received 8 November 2018; Revised 14 January 2019; Accepted 28 January 2019; Published 10 February 2019

Academic Editor: Pavel Lejcek

Copyright © 2019 Fu-qiang Yang et al. This is an open access article distributed under the Creative Commons Attribution License, which permits unrestricted use, distribution, and reproduction in any medium, provided the original work is properly cited.

Nuclear structural material austenitic stainless steel 316L is a polycrystalline composed of single crystals with a face-centered cubic (FCC) structure, and the intergranular stress corrosion cracking (IGSCC) is closely related to the crystal orientation. A constitutive model is presented to assess the elastic response of anisotropic behavior of single crystals in 316L in this study. With a bicrystal model built by the finite element method, the effects of crystal orientation and grain boundary (GB) inclination on the stress state nearby a symmetric tilt GB were discussed under the constant-displacement condition. The results indicate that when tensile axes are perpendicular to the GB, the stress and strain are equal at the GB and inside the grain, and the crystal misorientation has little effects on the stress and strain distribution. If the GB is not perpendicular to the load direction, the GB inclination angle will change the equivalent elastic modulus along the load direction and result in a larger stress in the grain with larger equivalent elastic modulus, but the stress tends to be equal inside the two grains. The grain size effects verification shows that the conclusions are independent of grain size.

## 1. Introduction

Internal structures and pipes in nuclear power plants (NPPs) are mainly made of austenitic stainless steels because of their good mechanical properties and resistance to corrosion, the degradations of these properties are observed under high-temperature, high-pressure, and neutron irradiation circumstances, and the intergranular stress corrosion cracking (IGSCC) is one of them [1–3], which seriously threatens the safety of NPPs. The IGSCC problems encountered with austenitic alloys in the nuclear industry motivated researchers to develop predictive models for IGSCC as a long-standing goal [4–6]. Besides the applied stress and corrosive environments, it has been widely observed that, for austenitic stainless steels, the susceptibility to IGSCC is significantly affected by the microstructure; particularly, it is

determined by the crystallography of the grain boundaries (GBs) [7–9]. Therefore, it is imperative that local behavior nearby GBs be identified in predicting the intergranular degradation.

The coincidence site lattice (CSL) model based upon Brandon's criterion, which assumes that certain deviations from the exact CSL misorientation could be accommodated by arrays of dislocations, is widely employed to describe grain boundary character distribution (GBCD). According to this model, low- $\Sigma$  CSL boundaries (CSLBs,  $\Sigma = 1-29$ ) were classified as "special," which are deviated from "random" or "general" high-angle boundaries (HABs) according to their exhibit properties (low interfacial energy and highly anisotropic interfacial energy), where  $\Sigma$  denotes the reciprocal density of coincident sites at the GB between two adjoining grains. Many researches have concluded that low- $\Sigma$  CSLBs,

including low-angle boundaries (LABs, or  $\Sigma 1$ ), are more resistant to IGSCC and other degradations such as cavitation, sensitization, and fracture [7, 10–13]. Researches have attributed the reason to the low boundary energies resulting in less impurity segregation, higher resistance to oxidation, and crack nucleation and propagation. Until recently, grain boundary engineering (GBE) studies for austenitic stainless steels have been performed to optimize the GBCD by improving the fraction of “special” GBs and reducing the random boundaries [14–19]. The IGSCC of 316L stainless steels and nickel-based alloy 690 in supercritical water was considerably reduced by the GBE based on the GBCD control increasing fraction of LABs and  $\Sigma 3$  CSLBs [17].

Unfortunately, not all the special GBs seem immune to IGSCC. Misorientations of the cracked LABs with  $12.8^\circ$ ,  $12.5^\circ$ ,  $13.0^\circ$ , and  $14.0^\circ$  in alloy 600,  $8.0^\circ$  in the 304 steel sample, and  $10.7^\circ$  in the 316 steel sample were observed [13]. Only except  $\Sigma 3$  of the special GBs, the  $\Sigma 9$  and  $\Sigma 27$  were also found to crack in a thermally sensitized type 304 austenitic steel in simulated pressurized water reactor environments [13], while 10% of the cracked boundaries were  $\Sigma 3$  in IGSCC during an in situ SCC experiment on a thermally sensitized type 304 stainless steel, tested in acidified potassium tetrathionate solution [20]. Moreover, contradictory results were observed that the best resistance to sensitization was of the deformed AISI 304L (by more than 80%) specimens, which have the lowest CSL fraction or the highest random boundaries, and suggested that extreme randomization of grain boundaries could be an alternative to achieve sensitization-resistant stainless steel [14, 21].

On account of IGSCC observed in both low- $\Sigma$  CSLBs and high- $\Sigma$  CSLBs, the environmental conditions and applied stress could also promote crack propagation together with the GB types and crystal orientation. So only acquiring the GB statistical characteristics and optimizing the GBCD are not enough to understanding the mechanism of IGSCC, and the stress and strain state nearby individual GBs should also be considered [22]. On performing the experiment on the pure copper bicrystals with a symmetrical 111-tilt boundary by the slow strain rate technique (SSRT) in 1M NaNO<sub>2</sub> solutions, it was found that small-angle tilt bicrystals fractured in a transgranular and intergranular manner, while large-angle bicrystals with misorientation larger than  $20^\circ$  fractured in an intergranular manner. The susceptibility to IGSCC appears to depend on the misorientation rather than the GB energy. The local stress concentration at HABs could be attributed to the high susceptibility to the IGSCC [23].

Considering the typicality of boundaries in real alloys, the IGSCC in single GBs in a 304 stainless steel was generated and monitored by using cantilevers manufactured by the focused ion beam (FIB) and tested by nanoindentation, which was expected to provide a more accurate method of measuring the crack growth and investigate the dependence of SCC resistance of single GBs on GB character and composition [24]. Despite the method with FIB enables researches to investigate the IGSCC in single GBs [24–27], it is difficult to manufacture specific single grain boundaries with respect to the irregularity of GBs and accurately measure the stress and strain

distribution nearby GBs. Thus, the elastic response of an isotropic behaviors of the austenitic stainless steel crystal was presented by a constitutive model, and the effects of crystal orientation on the stress state near the GB were studied by the finite element method [28]. In this paper, a three-dimensional anisotropic finite element analysis, which focuses on the bicrystal with a symmetric tilt GB, is performed to obtain how crystal orientation and grain boundary inclination affect the stress state nearby the GB of the bicrystal.

## 2. Crystallographic Constitutive Model

Austenitic stainless steels 316L is a polycrystalline material composed of single crystals with a face-centered cubic (FCC) structure. The elastic stress and strain relationship of single crystals is described by generalized Hooke's law:

$$\sigma = D\varepsilon, \quad (1)$$

where  $\sigma$  and  $\varepsilon$  denote the stress tensor and strain tensor, respectively, and  $D$  is the stiffness matrix, defined as follows:

$$D = \begin{bmatrix} d_{11} & d_{12} & d_{13} & & & \\ d_{21} & d_{22} & d_{23} & & & \\ d_{31} & d_{32} & d_{33} & & & \\ & & & d_{44} & & \\ & & & & d_{55} & \\ & & & & & d_{66} \end{bmatrix}, \quad (2)$$

where  $d_{ij}$  ( $i, j = 1, 2, \dots, 6$ ) is the elastic constant with  $d_{11} = d_{22} = d_{33}$ ,  $d_{44} = d_{55} = d_{66}$ , and  $d_{12} = d_{13} = d_{23} = d_{21} = d_{31} = d_{32}$ .

The elastic modulus  $E$ , Poisson's ratio  $\mu$ , and shear modulus  $G$  in the three main axes  $\langle 100 \rangle$  of the single crystal material with FCC could be calculated as

$$E = \frac{(d_{11} - d_{12}) \cdot (d_{11} + 2d_{12})}{d_{11} + d_{12}},$$

$$\mu = \frac{d_{12}}{d_{11} + d_{12}}, \quad (3)$$

$$G = d_{44}.$$

The elastic modulus of the single crystal in  $\langle 110 \rangle$  and  $\langle 111 \rangle$  crystal orientations can be described as

$$E_{110} = \frac{4GE}{E + 2G(1 - \mu)}, \quad (4)$$

$$E_{111} = \frac{3GE}{E + G(1 - 2\mu)}.$$

In a polycrystalline material, the crystal coordinate and global coordinate are always different, and the stress and strain should be recalculated with the rotation stiffness matrix  $D^{xyz}$ :

$$D^{xyz} = ADA^T, \quad (5)$$

where  $A$  is the rotation matrix, defined as follows:

$$A = \begin{bmatrix} l_1^2 & m_1^2 & n_1^2 & 2l_1m_1 & 2l_1n_1 & 2m_1n_1 \\ l_2^2 & m_2^2 & n_2^2 & 2l_2m_2 & 2l_2n_2 & 2m_2n_2 \\ l_3^2 & m_3^2 & n_3^2 & 2l_3m_3 & 2l_3n_3 & 2m_3n_3 \\ l_1l_2 & m_1m_2 & n_1n_2 & l_1m_2 + l_2m_1 & l_1n_2 + l_2n_1 & m_1n_2 + m_2n_1 \\ l_1l_3 & m_1m_3 & n_1n_3 & l_1m_3 + l_3m_1 & l_1n_3 + l_3n_1 & m_1n_3 + m_3n_1 \\ l_2l_3 & m_2m_3 & n_2n_3 & l_2m_3 + l_3m_2 & l_2n_3 + l_3n_2 & m_2n_3 + m_3n_2 \end{bmatrix}, \quad (6)$$

where  $l_i$ ,  $m_i$ , and  $n_i$  ( $i, j = 1, 2, \dots, 6$ ) are the direction cosines between the crystal coordinate and global coordinate.

### 3. Finite Element Model

**3.1. Material Model of Bicrystals.** The elastic anisotropy of stainless steel 316L single crystals is modelled using the elastic constants,  $d_{11} = 204.6$  GPa,  $d_{12} = 137.7$  GPa, and  $d_{44} = 126.2$  GPa [29]. By substituting elastic constants into (3) ~ (7), the elastic modulus  $E$ , shear modulus  $G$ , and Poisson's ratio  $\mu$  are 94.06 GPa, 126.2 GPa, and 0.402, respectively. The elastic modulus along  $\langle 110 \rangle$  and  $\langle 111 \rangle$  orientations is 193.81 GPa and 299.77 GPa, respectively. For FCC single crystals, the highest elastic stiffness is along the  $\langle 111 \rangle$  orientations, the lowest stiffness is along the  $\langle 100 \rangle$  orientations, and  $E_{111} > E_{110} > E_{100} = E$  could be acquired, as shown in Figure 1.

In order to gain a deeper understanding of GBs characterization, a bicrystal with a symmetric tilt GB is involved. As shown in Figure 2, it is assumed that the two adjacent grains (grains A and B) have the same orientation with the  $[001]$  direction coincidence to the 3-axis of the global coordinate initially, or the  $(001)$  plane of the crystal parallel to the 1-2 plane in the global coordinate. By rotating the two adjacent grains (grains A and B) around the  $[001]$  direction with  $\pm\theta/2$ , respectively, the angle between GB and  $[010]$  direction of each grain is  $\theta/2$ ; thus, a symmetric tilt GB with crystal misorientation equal to  $\theta$  is formed, and the angle  $\alpha$  between 1-axis and GB normal is defined as the GB inclination angle, which is in the range of  $[0^\circ, 90^\circ]$ .  $\varphi_A$  and  $\varphi_B$  are the angles between  $[110]$  orientation and 1-axis for grain A and grain B, respectively. The orientation of each grain is defined in the FEM by rotating the material coordinates.

**3.2. Geometry Model and Boundary Condition.** Two types of GB are modelled in bicrystals; the type I GB shown in Figure 3 is perpendicular to tensile axes, and the type II GB has a GB inclination angle  $\alpha$  in the range of  $[0^\circ, 90^\circ]$ , as shown in Figure 4. Influenced by aging time, temperature, and other factors, the average grain size of 316L stainless steels varies from  $17 \mu\text{m}$  to  $200 \mu\text{m}$  in the literature [19, 30]; thus, the dimension of each component grain is assumed to be  $20 \mu\text{m} \times 20 \mu\text{m} \times 50 \mu\text{m}$  arbitrarily.

The surface perpendicular to 1-axis of grain A is fixed initially, followed by setting constant displacement  $U_1$  equal to  $0.5 \mu\text{m}$  along 1-axis applied on the right surface of grain B,

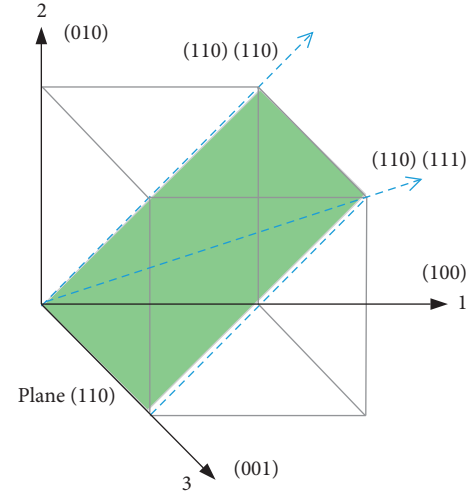


FIGURE 1: Selected FCC single crystal directions for analysis.

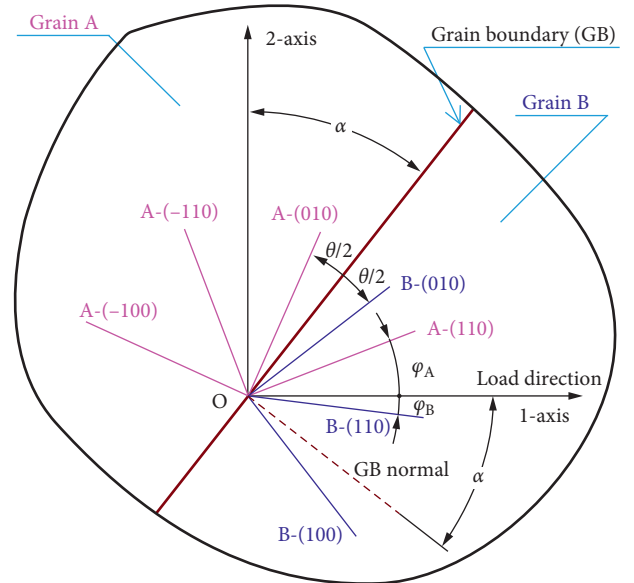


FIGURE 2: Orientations of two adjacent grains in bicrystals.

and this causes a total strain of 0.5% along 1-axis for the whole bicrystal.

**3.3. Mesh Model.** The calculation scale and calculation accuracy are the main factors concerned when establishing the finite element model in this simulation. It is known that a dense mesh acquired by increasing the mesh numbers can better reflect the data change gradient and improve the calculation accuracy; however, it will also increase the calculation scale simultaneously. This study focuses on the stress distribution nearby the GB; thus, a fine meshing was carried out at GBs to acquire more accurate stress and strain. To balance the calculation scale and calculation accuracy when meshing, a trial calculation with a coarse mesh was carried out arbitrarily to acquire a short calculation time, and then a more elaborate mesh was taken. If there is only a



TABLE 1: Seed strategy in the mesh model (seed by size).

Number	Seed density ( $\mu\text{m}$ )			Mesh size ( $\mu\text{m}$ )		Aspect ratio	Total mesh number	Time consumed (s)
	Edge list 1	Edge list 2	Edge list 3	Min.	Max.			
1	0.5	0.5-4	0.5	$0.5 \times 0.5 \times 0.5$	$0.5 \times 0.5 \times 4$	5	102400	152
2	0.2	0.2-4	0.5	$0.5 \times 0.5 \times 0.2$	$0.5 \times 0.5 \times 4$	8	150400	282

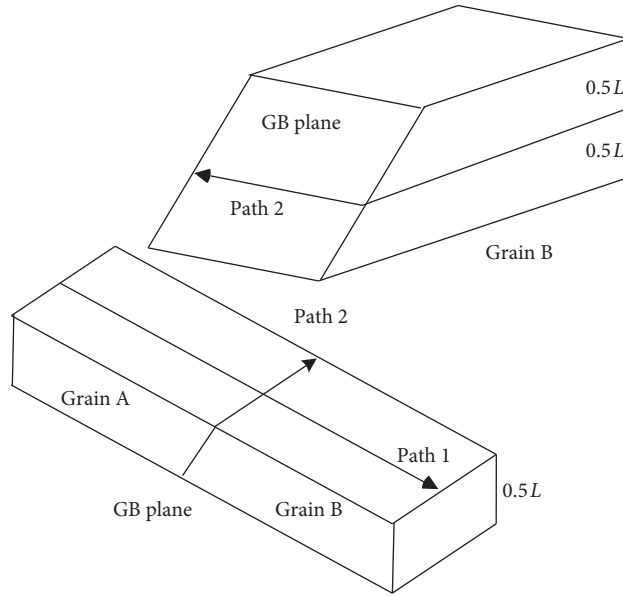


FIGURE 6: Locations of the two paths to measure stress.

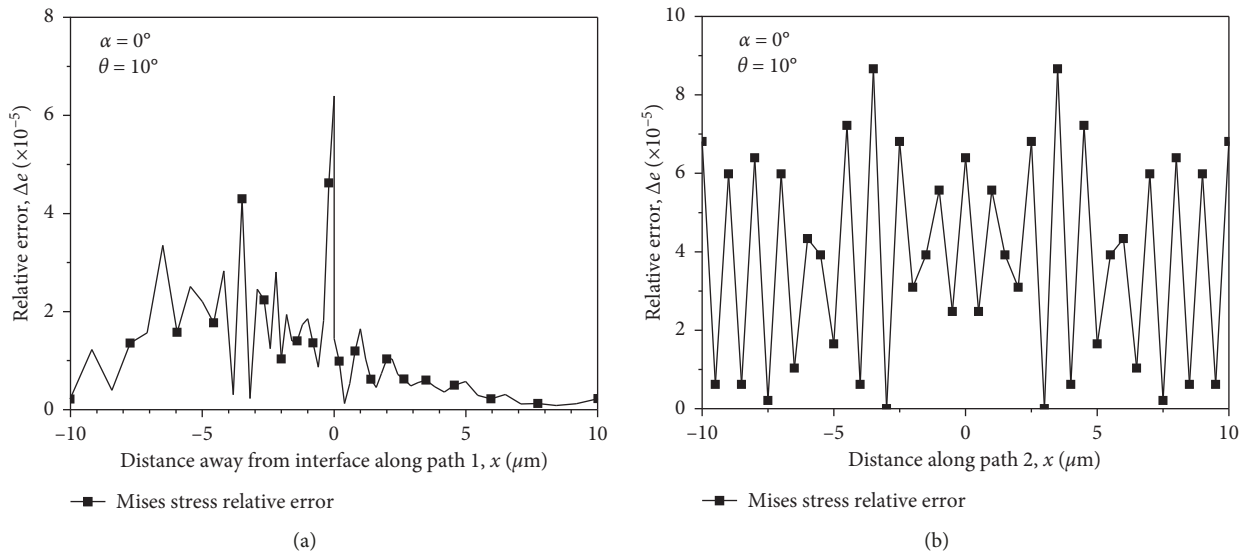


FIGURE 7: Calculation error between two mesh strategies.

distribution of a single crystal beam is shown in Figure 8. It can be seen that, along path 1, the Mises stress impulses from 185 MPa to 547 MPa and then decreases to a stable value about 477 MPa when  $x > -25 \mu\text{m}$ . According to the stress distribution on the cross section, it can be seen that, on the fixed end with  $x = -25 \mu\text{m}$ , the outer contour has a larger Mises stress than the inner contour, and the ratio of the

maximum value at the corners and minimum value in the center is about 3.6. With the increase of the  $x$  value, the Mises stress distribution on the cross section changes and leads to the ratio of Mises stress at the corner and center on the cross section equal to 1, with respect to the uniform distribution of Mises stress on the cross section. The Mises stress distribution shown in Figure 8 demonstrates the

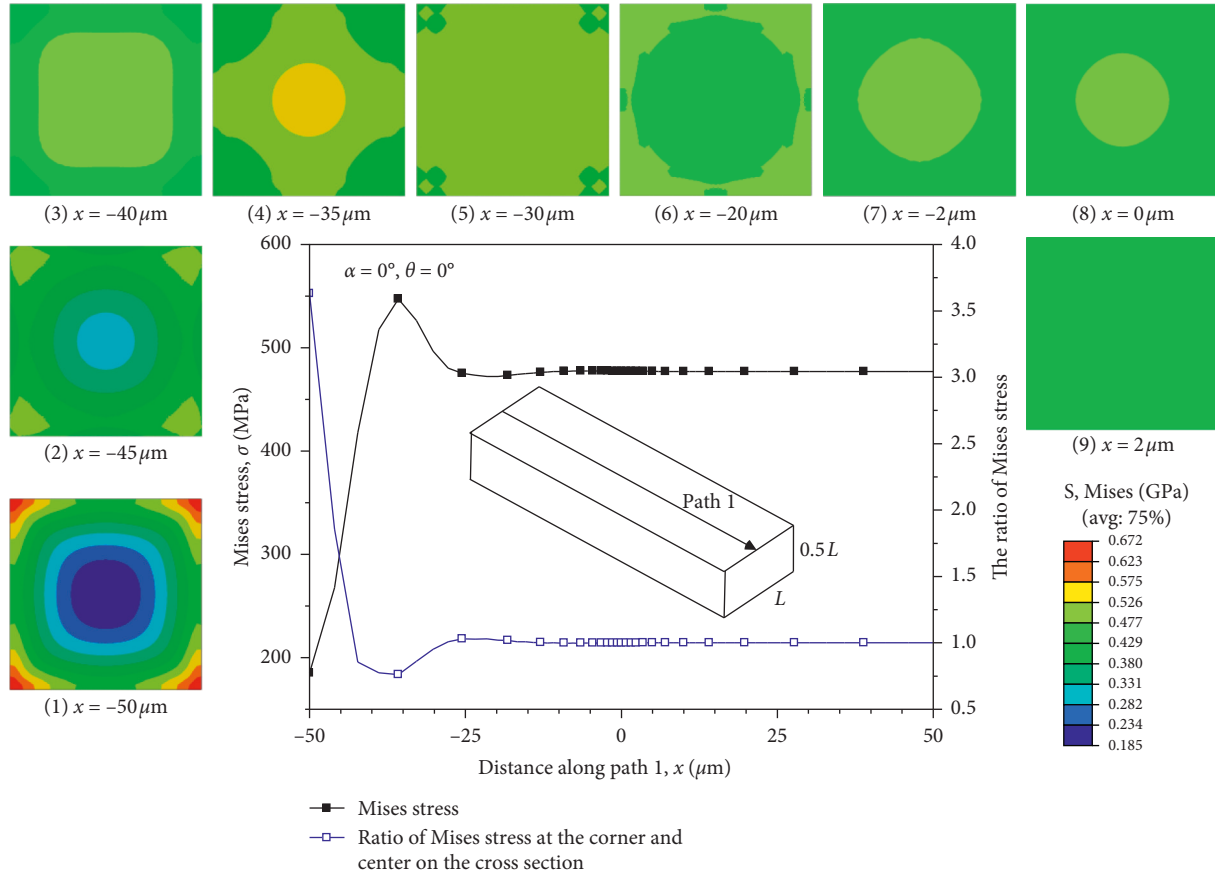


FIGURE 8: Stress distribution in a single crystal beam.

uniaxial tensile elastic response of a beam with the fixed-end constraint, that the stress concentration exists at the fixed end, and that the stress tends to uniform distribution far from the fixed end. As the model is simplified as a single crystal beam, the strain could be calculated according to (1), and the strain distribution is neglected due to the same distribution tendency with stress.

**4.2. Bicrystals with Type I GB.** For bicrystals with type I GB, the GB inclination angle  $\alpha$  is equal to 0. The misorientation of LABs is below  $10^\circ$ ; thus,  $\theta$  is in the range of  $0^\circ \sim 10^\circ$  for a symmetric tilt GB. If  $\theta$  is equal to  $0^\circ$ , the two adjacent grains have the same orientation and result in a single crystal material. To study the stress state caused by misorientations between grain A and grain B, a stress scale factor  $\lambda$  is introduced to normalize the stress as follows:

$$\lambda = \frac{\text{actual stress}}{\text{reference stress}}, \quad (7)$$

where the actual stress and reference stress are observed along path 1 and path 2, as shown in Figure 6. The reference stress is acquired when  $\theta$  equals  $0^\circ$ .

The average value and standard deviation of Mises stress scale factors within  $10 \mu\text{m}$  of the GB along path 1 with different grain misorientations are shown in Figure 9; the standard deviation is very small, which indicates that the

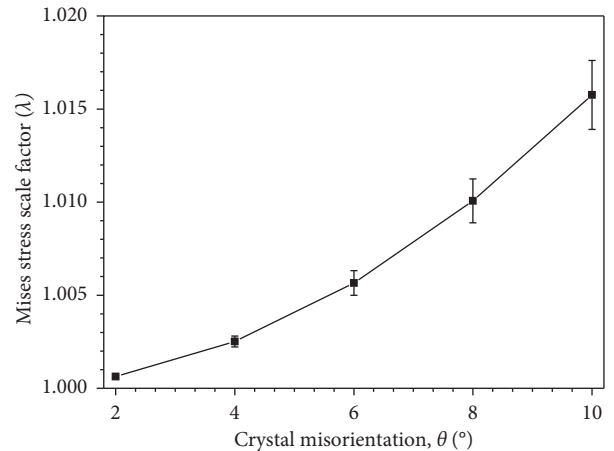


FIGURE 9: Mises stress scale factors along path 1 for type I bicrystals.

Mises stress is almost equivalent inside both grains and on the GB at a certain crystal orientation; this could be explained by the symmetric orientations of two grains with respect to the GB, which leads to the same equivalent elastic modulus  $E_{\text{equ}}$  of two grains along 1-axis, and thus, the equivalent stress could be observed with constant displacement. Even with the same equivalent elastic modulus  $E_{\text{equ}}$ , the stress distribution on both sides of the GB is asymmetric and inconsistent, and a slight difference exists

due to the bicrystal beam having a fixed-end constraint, which will lead to the stress inconsistency even in a single crystal material, as shown in Figure 8; the standard deviation interprets the stress inconsistency caused by the asymmetric boundary conditions and load conditions. The Mises stress scale factor increases with the increase of crystal misorientation, accompanied by an increase in the gradient, which denotes a higher Mises stress inside the bicrystal with a larger crystal misorientation. Considering the anisotropy of single crystals,  $E_{110} > E_{100}$ , and the stress is larger in  $\langle 110 \rangle$  orientation than  $\langle 100 \rangle$  orientation with the same displacement load applied along the crystal orientation. An equivalent elastic modulus  $E_{\text{equ}}$  along the load direction can be calculated if the load direction is between  $\langle 110 \rangle$  and  $\langle 100 \rangle$  directions, and there is  $E_{110} > E_{\text{equ}} > E_{100}$ . A larger equivalent elastic modulus along the load direction can be acquired if the angle between tensile axes and  $[110]$  orientation is small. The increase of  $\theta$  will reduce the angle between  $[110]$  orientation and load direction and lead to the increase of equivalent elastic modulus along the load direction. Finally, the stress is larger in bicrystals with larger crystal misorientations under the same strain state according to (1).

Let  $\bar{\epsilon}_{xA}$  and  $\bar{\epsilon}_{xB}$  represent the average strain  $\epsilon_x$  of component grains A and B along path 1, and let  $\epsilon_{xA}$  and  $\epsilon_{xB}$  represent the average strain of all elements along path 2 on the GB in component grains A and B, respectively. The deformation nearby the GB of bicrystals shown in Figure 10 illustrates that the strain on the GB of each grain is equal; this could be induced by the equal equivalent elastic modulus and stress applied nearby the GB. The average strain of grain B is slightly larger than that of grain A; this may be caused by the asymmetric boundary condition and load applied. By increasing the crystal misorientation, the strain at the GB increases a little, along with a slight increase and decrease of average strain in grain A and grain B, respectively.

Note that when  $\theta$  changes from  $0^\circ$  to  $10^\circ$ , the stress scale factor is no more than 1.016 in Figure 9, and the strain changes are also very small in Figure 10, which indicates that the crystal misorientation has little effects on the distribution of stress and strain in bicrystals with type I symmetric tilt GB.

**4.3. Bicrystals with Type II GB.** Assuming the crystal misorientation equal to  $10^\circ$ , the stress and strain distribution in bicrystals with type II GB was calculated. When the GB inclination angle  $\alpha = 0^\circ$ , the GB is perpendicular to tensile axes, and the type II GB will change to type I GB; thus, the stress calculated at  $\theta = 10^\circ$  and  $\alpha = 0^\circ$  is used in (7) as reference stress in the following.

Figures 11 and 12 illustrate the stress scale factor within  $25 \mu\text{m}$  of the GB and on the GB, respectively. When the GB inclination angle is equal to  $15^\circ$ , the stress scale factors are greater than 1 along path 1, which indicates that the stress increases inside the grains and on the grains with a tilt GB. The stress is higher in grain B than in grain A near the GB, but the stress differences reduce and tend to equal far away from the GB in both grains. The stress scale factor has the similar variation with GB inclination angle equal to  $30^\circ$ . In spite of a higher stress scale factor appearing when GB

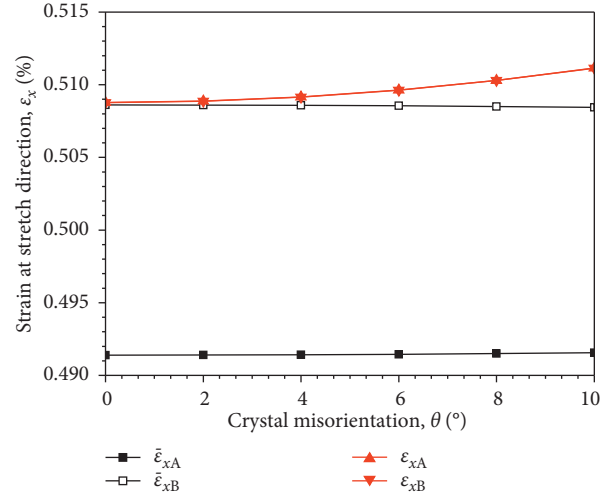


FIGURE 10: Strain state of each grain for type I bicrystals.

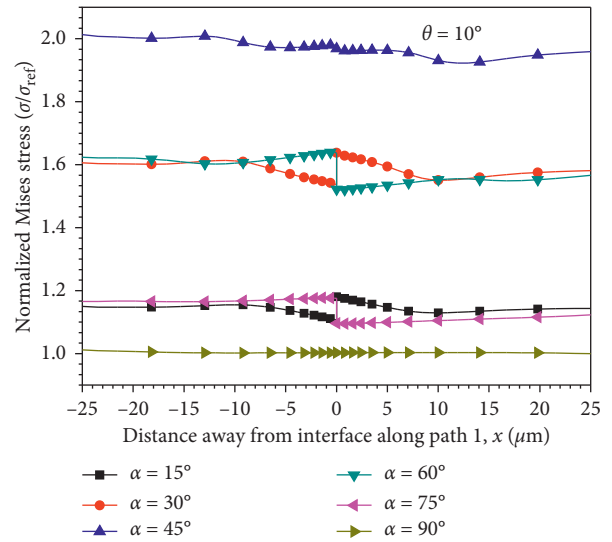


FIGURE 11: Mises stress scale factors along path 1 for type II bicrystals.

inclination angle is equal to  $45^\circ$ , the stress difference at the GB decreases. When the GB inclination angle increases from  $45^\circ$  to  $75^\circ$ , an opposite stress distribution in grain A and grain B is obtained. To understand this phenomenon, equations (8) and (9) are evolved according to Figure 2, as follows:

$$\varphi_A = 45^\circ - \left( \alpha - \frac{\theta}{2} \right), \quad (8)$$

$$\varphi_B = 45^\circ - \left( \alpha + \frac{\theta}{2} \right), \quad (9)$$

where  $\varphi_A$  and  $\varphi_B$  are the angles between  $[110]$  orientation and 1-axis for grain A and grain B, respectively.

The angles between tensile axes and  $[110]$  orientation for grain A and grain B with different GB inclination angles are listed in Table 2, which illustrates that when GB inclination angle increases to  $15^\circ$  or  $30^\circ$ ,  $\varphi$  decreases in both grains and

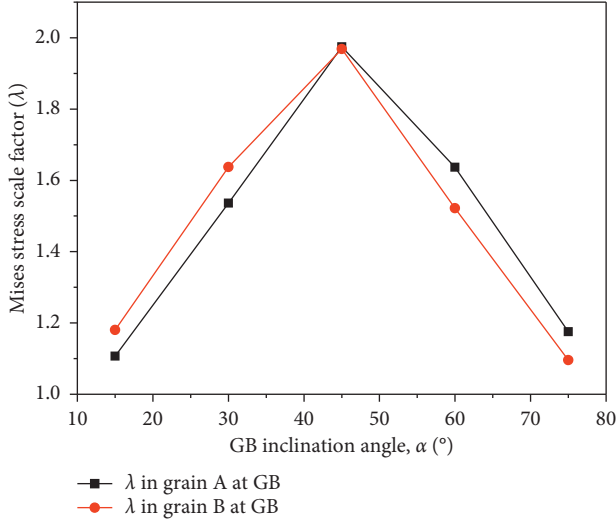


FIGURE 12: Mises stress scale factors on the boundary for type II bicrystals.

TABLE 2: Angles between [110] orientation and 1-axis changes with different GB inclination angles.

GB inclination angle, $\alpha$ (°)	Crystal misorientation, $\theta$ (°)	Angles between [110] and 1-axis changes	
		$\varphi_A$ (°)	$\varphi_B$ (°)
15	10	35	25
30	10	20	10
45	10	5	-5
60	10	-10	-20
75	10	-25	-35

$\varphi_B > \varphi_A$ . This causes the equivalent elastic modulus  $E_{equ}$  of grain A and grain B to increase, and a larger equivalent elastic modulus occurs in grain B than in grain A. Finally, the stress of grain B is greater than that of grain A, and the stress scale factor increases when GB inclination angle increases to 15° or 30°. When the GB inclination angle increases to 45°, it results in  $|\varphi_A| = |\varphi_B| = 5^\circ$ , and thus, the adjacent two grains have the same equivalent elastic modulus and lead to the same stress in two grains.

The stress scale factor shows a decrease when GB inclination angle increases from 45° to 75°, and this is also caused by the decrease of angle between tensile axes and [110] orientation. Contrary to the stress at the GB with  $0^\circ < \alpha < 45^\circ$ , the stress of grain A is higher than that of grain B. Comparing the stress scale factor at  $\alpha = 15^\circ$  and  $\alpha = 75^\circ$ , or  $\alpha = 30^\circ$  and  $\alpha = 60^\circ$ , opposite distribution of stress scale factor could be found along path 1; this is induced by the exchange of angle between tensile axes and [110] orientation for grain A and grain B. When GB inclination angle increases to 90°, the GB plane is parallel to the tensile axes, and the stress scale factor is approximately equal to 1.

The average strain along path 1 and the strain on the GB of each grain are shown in Figure 13. The average strain  $\bar{\epsilon}_{xA}$  equals to  $\bar{\epsilon}_{xB}$  for two grains when  $\alpha = 45^\circ$ ; this is because they

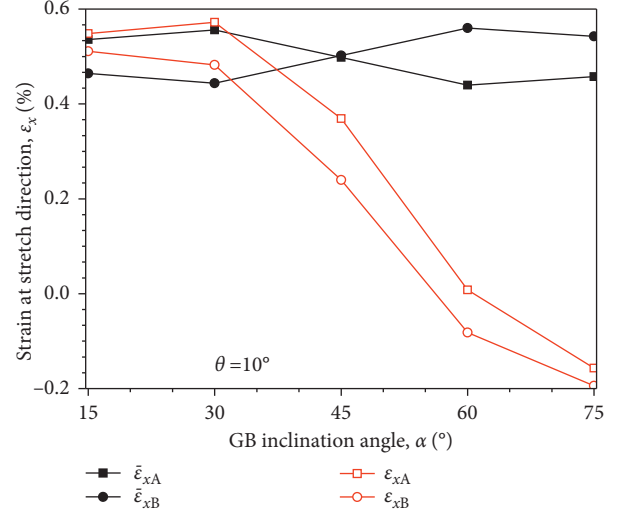


FIGURE 13: Strain state at the grain boundary and average strain of each grain for type II bicrystals.

have the same angle between tensile axes and [110] orientation. The average strain of grain A is larger than that of grain B when  $\alpha < 45^\circ$ , and the opposite results can be obtained with  $\alpha > 45^\circ$ . The strain of grain A is larger than that of grain B at the GB with  $\alpha = 15^\circ$ . The strain in both grains at the GB decreases with the increase of GB inclination angle and decreases gradually to 0 at  $\alpha$  approximately equal to 60°. The strain will reduce to negative values if  $\alpha$  increases continuously. The strain changes from positive to negative, which denotes that the strain state of the grain changes from tensile to compression in the load direction. And now, the strain of grain B is larger than that of grain A.

**4.4. Grain Size Independence Test.** It is arbitrarily assumed that each component grain is  $20 \mu\text{m} \times 20 \mu\text{m} \times 50 \mu\text{m}$  in this simulation, and thus, another verification simulation, with a bigger geometric size of each component grain equal to  $40 \mu\text{m} \times 40 \mu\text{m} \times 100 \mu\text{m}$ , was carried out to discuss the grain size effects on the simulation results. The verification model has the same material model, mesh strategy, and boundary conditions. In order to model an identical loading condition of a total strain equal to 0.5% along 1-axis for the whole bicrystal, a constant displacement  $U_1$  equal to  $1 \mu\text{m}$  was also applied on the right surface of grain B along 1-axis. The effects of the grain size are shown in Figure 14, in which the Mises stress differences were observed along path 1 and path 2 defined in Figure 6. It can be seen that, with different grain sizes, the relative differences of Mises stress within  $10 \mu\text{m}$  on both sides of the GB are smaller than 0.6%, and the relative differences on normalized distance along path 2 are also smaller than 2%. Thus, it is concluded that the calculation results in this study are independent of grain size.

## 5. Conclusions

A constitutive model has been presented to assess the elastic response of anisotropic behavior of single crystals in

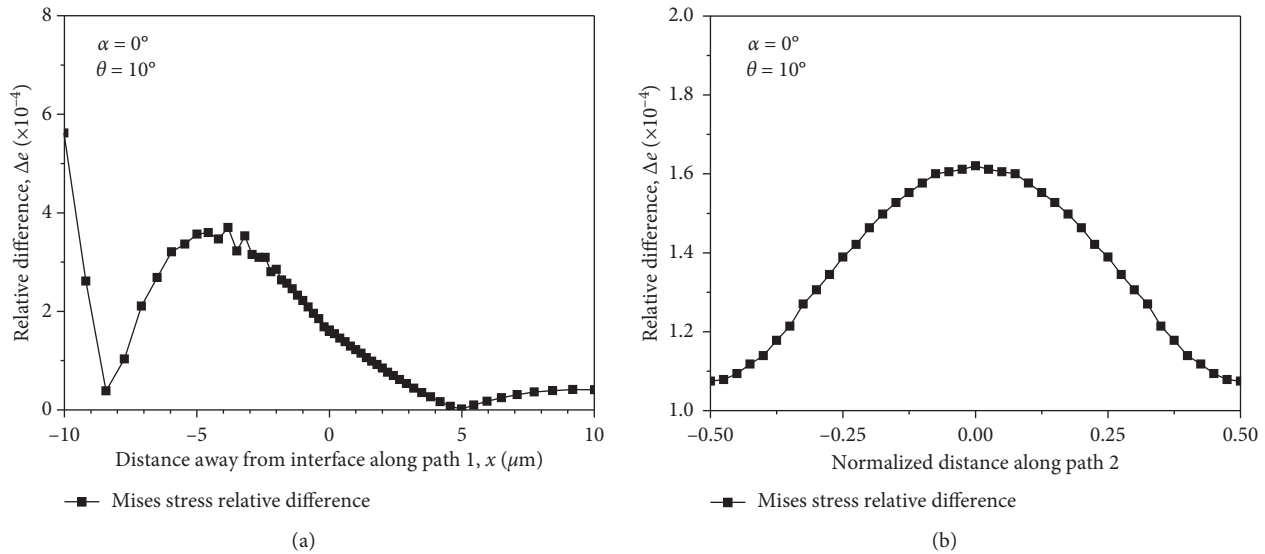


FIGURE 14: Grain size effect on calculation results.

austenitic stainless steel 316L. The FEM has been used to determine how the crystal orientation and GB inclination affect the stress state nearby the symmetric tilt GB. The results indicate that the stress and strain are equal at the GB and inside the grain, and the crystal misorientation of the symmetric tilt GB has little effects on the stress and strain distribution when tensile axes are perpendicular to the GB. For bicrystals with the GB not perpendicular to the load direction, the change of GB inclination angle will change the equivalent elastic modulus along the load direction and lead to the stress and strain inhomogeneity at the GB. The stress is larger on the side which has larger equivalent elastic modulus, but the stress tends to be equal inside the two grains. Even with the GB inclination to tensile axes, the stress at the boundary or inside the grain may have the same value if it leads to the same equivalent elastic modulus at both sides. Thus, it could be concluded that the stress distribution of bicrystals composed by anisotropic single crystals is affected by crystal orientation and GB inclination simultaneously, and the results are independent of grain size.

### Data Availability

The data used to support the findings of this study were calculated according to the finite element method, and they are included within the article. The elastic constants of 316L single crystals used in the calculation model were cited from Reference [29].

### Conflicts of Interest

The authors declare that there are no conflicts of interest regarding the publication of this paper.

### Acknowledgments

This work was supported by the Research Fund of State Key Laboratory for Marine Corrosion and Protection of Luoyang

Ship Material Research Institute (LSMRI) (Contract no. 61429010102), the National Natural Science Foundation of China (Grant nos. 51775427 and 51475362), the Key Research and Development Program of Shaanxi Province (Grant no. 2017GY-034), and the Natural Science Basic Research Plan in Shaanxi Province of China (Grant no. 2018JQ5193).

### References

- [1] R. M. Horn, G. M. Gordon, F. P. Ford, and R. L. Cowan, "Experience and assessment of stress corrosion cracking in L-grade stainless steel BWR internals," *Nuclear Engineering and Design*, vol. 174, no. 3, pp. 313–325, 1997.
- [2] P. J. Kentish, "Gas pipeline failures: Australian experience," *British Corrosion Journal*, vol. 20, no. 3, pp. 139–146, 2013.
- [3] A. Stratulat, J. A. Duff, and T. J. Marrow, "Grain boundary structure and intergranular stress corrosion crack initiation in high temperature water of a thermally sensitised austenitic stainless steel, observed in situ," *Corrosion Science*, vol. 85, no. 1, pp. 428–435, 2014.
- [4] R. N. Parkins, "Predictive approaches to stress corrosion cracking failure," *Corrosion Science*, vol. 20, no. 2, pp. 147–166, 1980.
- [5] F. P. Ford, "Quantitative prediction of environmentally assisted cracking," *Corrosion*, vol. 52, no. 5, pp. 375–395, 1996.
- [6] F. Q. Yang, H. Xue, L. Y. Zhao, and X. R. Fang, "A quantitative prediction model of SCC rate for nuclear structure materials in high temperature water based on crack tip creep strain rate," *Nuclear Engineering and Design*, vol. 278, pp. 686–692, 2014.
- [7] T. Watanabe, "An approach to grain boundary design of strong and ductile polycrystals," *Res Mechanica*, vol. 11, no. 1, pp. 47–84, 1984.
- [8] G. Palumbo, P. J. King, K. T. Aust, U. Erb, and P. C. Lichtenberger, "Grain boundary design and control for intergranular stress-corrosion resistance," *Scripta Metallurgica et Materialia*, vol. 25, no. 8, pp. 1775–1780, 1991.
- [9] E. M. Lehockey, A. M. Brennenstuhl, and I. Thompson, "On the relationship between grain boundary connectivity,

- coincident site lattice boundaries, and intergranular stress corrosion cracking,” *Corrosion Science*, vol. 46, no. 10, pp. 2383–2404, 2004.
- [10] G. Palumbo, E. M. Lehockey, and P. Lin, “Applications for grain boundary engineered materials,” *JOM*, vol. 50, no. 2, pp. 40–43, 1998.
- [11] D. C. Crawford and G. S. Was, “The role of grain boundary misorientation in intergranular cracking of Ni-16Cr-9Fe in 360°C argon and high-purity water,” *Metallurgical Transactions A*, vol. 23, no. 4, pp. 1195–1206, 1992.
- [12] J. Lu and J. A. Szpunar, “Microstructural model of intergranular fracture during tensile tests,” *Journal of Materials Processing Technology*, vol. 60, no. 1, pp. 305–310, 1996.
- [13] V. Y. Gertsman and S. M. Bruemmer, “Study of grain boundary character along intergranular stress corrosion crack paths in austenitic alloys,” *Acta Materialia*, vol. 49, no. 9, pp. 1589–1598, 2001.
- [14] M. Shimada, H. Kokawa, Z. J. Wang, Y. S. Sato, and I. Karibe, “Optimization of grain boundary character distribution for intergranular corrosion resistant 304 stainless steel by twin-induced grain boundary engineering,” *Acta Materialia*, vol. 50, no. 9, pp. 2331–2341, 2002.
- [15] G. S. Was, B. Alexandreanu, P. Andresen, and M. Kumar, “Role of coincident site lattice boundaries in creep and stress corrosion cracking,” *MRS Proceedings*, vol. 819, pp. 1–14, 2004.
- [16] M. Michiuchi, H. Kokawa, Z. J. Wang, Y. S. Sato, and K. Sakai, “Twin-induced grain boundary engineering for 316 austenitic stainless steel,” *Acta Materialia*, vol. 54, no. 19, pp. 5179–5184, 2006.
- [17] E. A. West and G. S. Was, “IGSCC of grain boundary engineered 316L and 690 in supercritical water,” *Journal of Nuclear Materials*, vol. 392, no. 2, pp. 264–271, 2009.
- [18] S. Saito, K. Kikuchi, H. Dai et al., “Corrosion-erosion test of SS316L grain boundary engineering material (GBEM) in lead bismuth flowing loop,” *Journal of Nuclear Materials*, vol. 431, no. 1-3, pp. 91–96, 2012.
- [19] S. Kobayashi, R. Kobayashi, and T. Watanabe, “Control of grain boundary connectivity based on fractal analysis for improvement of intergranular corrosion resistance in SUS316L austenitic stainless steel,” *Acta Materialia*, vol. 102, pp. 397–405, 2016.
- [20] S. Rahimi, D. L. Engelberg, J. A. Duff, and T. J. Marrow, “In situ observation of intergranular crack nucleation in a grain boundary controlled austenitic stainless steel,” *Journal of Microscopy*, vol. 233, no. 3, pp. 423–431, 2010.
- [21] D. N. Wasnik, V. Kain, I. Samajdar, B. Verlinden, and P. K. De, “Resistance to sensitization and intergranular corrosion through extreme randomization of grain boundaries,” *Acta Materialia*, vol. 50, no. 18, pp. 4587–4601, 2002.
- [22] B. Alexandreanu and G. S. Was, “The role of stress in the efficacy of coincident site lattice boundaries in improving creep and stress corrosion cracking,” *Scripta Materialia*, vol. 54, no. 6, pp. 1047–1052, 2006.
- [23] H. Miyamoto, H. Koga, T. Mimaki, and S. Hashimoto, “Intergranular stress corrosion cracking of pure copper <111> tilt bicrystals,” *Interface Science*, vol. 9, no. 3-4, pp. 281–286, 2001.
- [24] D. E. J. Armstrong, M. E. Rogers, and S. G. Roberts, “Micromechanical testing of stress corrosion cracking of individual grain boundaries,” *Scripta Materialia*, vol. 61, no. 7, pp. 741–743, 2009.
- [25] H. Dugdale, D. E. J. Armstrong, E. Tarleton, S. G. Roberts, and S. Lozano-Perez, “How oxidized grain boundaries fail,” *Acta Materialia*, vol. 61, no. 13, pp. 4707–4713, 2013.
- [26] A. Stratulat, D. E. J. Armstrong, and S. G. Roberts, “Micro-mechanical measurement of fracture behaviour of individual grain boundaries in Ni alloy 600 exposed to a pressurized water reactor environment,” *Corrosion Science*, vol. 104, pp. 9–16, 2016.
- [27] D. E. J. Armstrong, A. J. Wilkinson, and S. G. Roberts, “Micro-mechanical measurements of fracture toughness of bismuth embrittled copper grain boundaries,” *Philosophical Magazine Letters*, vol. 91, no. 6, pp. 394–400, 2011.
- [28] F. Q. Yang, H. Xue, L. Y. Zhao, and X.-R. Fang, “Effects of grain orientation on stress state near grain boundary of austenitic stainless steel bicrystals,” *Advances in Materials Science and Engineering*, vol. 2018, Article ID 9409868, 10 pages, 2018.
- [29] H. M. Ledbetter, “Monocrystal-polycrystal elastic constants of a stainless steel,” *Physica Status Solidi A*, vol. 85, no. 1, pp. 89–96, 2010.
- [30] C. Y. Jeong, K. J. Kim, H. U. Hong, and S. W. Nam, “Effects of aging temperature and grain size on the formation of serrated grain boundaries in an AISI 316 stainless steel,” *Materials Chemistry and Physics*, vol. 139, no. 1, pp. 27–33, 2013.
- [31] Dassault Systèmes Simulia Corp., *Abaqus Analysis User’s Manual 6.12*, Dassault Systèmes Simulia Corp., Providence, RI, USA, 2012.



**Hindawi**  
Submit your manuscripts at  
[www.hindawi.com](http://www.hindawi.com)

